AIAA AVIATION Forum
17-21 June 2019, Dallas, Texas
AIAA Aviation 2019 Forum

10.2514/6.2019-3204

Energy- and Entropy-Stable Multidimensional Summation-by-Parts Discretizations on Non-Conforming Grids

Siavosh Shadpey* and David W. Zingg†
University of Toronto Institute for Aerospace Studies, Toronto, Ontario, M3H 5T6, Canada

We present three multidimensional summation-by-parts (SBP) discretization methods for the Euler equations which are applicable to non-conforming grids arising from h-adaptivity, p-adaptivity, or hp-adaptivity. The coupling of non-conforming elements is performed using high-order quadrature rules and interface interpolation and projection operators which preserve the design-order accuracy, element-wise conservation, and stability properties of the methods. The first scheme is based on linear energy analysis and is the most efficient of the three methods. The second scheme is entropy stable and compatible with diagonal-E SBP operators, which have collocated volume cubature and facet quadrature nodes. The third scheme is a generalization of the second: it is entropy stable and compatible with dense-E SBP operators. Numerical investigations verify the conservation, stability, and accuracy properties of the schemes. A brief study is also performed to compare the methods in terms of efficiency and robustness.

I. Introduction

High-order methods are computationally more efficient than low-order methods for simulations with stringent accuracy requirements, such as large eddy simulations and direct numerical simulations, since they can achieve the same error as their lower order counterparts on coarser grids [1, 2]. A few choices of high-order discretization methods are the flux reconstruction, discontinuous Galerkin, and summation-by-parts methods [3–5]. For systems of linear hyperbolic equations, some schemes belonging to these families can be shown to be *a priori* stable using the energy analysis. For nonlinear partial differential equations (PDEs), the energy analysis is often used to prove stability by first linearizing the equations about a (local) constant state and symmetrizing them via a change of variables [6]. Generally, the discretization of the original PDEs, and not the symmetrized PDEs, is implemented and, thus, the stability proof does not hold. Furthermore, for solutions with discontinuities, the proof is also nullified since the equations cannot be linearized [7]. It is possible to improve the stability of energy-stable schemes for nonlinear equations by introducing numerical dissipation. One way of doing this relies on user intervention to vary the amount of dissipation added on a case-by-case basis and can lead to solution contamination (i.e. too much dissipation) or to time instability (i.e. not enough dissipation) [8].

A more reliable and robust alternative is to use nonlinearly stable (or entropy-stable) numerical methods, which discretely satisfy an entropy inequality. Using a Galerkin formulation, this can be achieved when the entropy variables are in the finite-element space, as shown in [9, 10], and exact integration is performed. Unfortunately, the nonlinear fluxes of the compressible Navier-Stokes equations are not polynomial functions and, thus, cannot be exactly integrated using polynomial-based cubature rules. In 2012, Fisher [7] developed high-order nonlinearly stable methods for the Navier-Stokes equations without relying on exact integration. The key foundations of his work were entropy-conservative numerical fluxes, such as Ismail and Roe's [11], and finite-difference Summation-by-Parts (SBP) methods, which discretely mimic integration-by-parts. This mimetic property, known as the SBP property, is extensively used to prove discrete conservation and time stability. More recently, Fisher's framework has been extended to include tensor-product discontinuous spectral collocation methods [12], simplex meshes [13–15], staggered grids [16, 17], space-time discretization methods [18], and various entropy-stable boundary conditions [19, 20]. Although entropy-stable methods possess *a priori* nonlinear stability, they approximate the derivative of the flux using relatively expensive entropy-conservative fluxes, which renders them computationally more costly than energy-stable methods. Ideally, entropy-stable schemes are to be coupled with output-based *a posteriori* error estimates in order to achieve user-requested error tolerances in an automated, robust, reliable, and efficient manner by adaptively refining the mesh [21–23]. In a

*Graduate Student, Institute for Aerospace Studies (sia.shadpey@mail.utoronto.ca)
†University of Toronto Distinguished Professor of Computational Aerodynamics and Sustainable Aviation, Director, Centre for Sustainable Aviation, Director, Centre for Computational Science and Engineering, Institute for Aerospace Studies and Associate Fellow AIAA

step towards this direction, Friedrich et al. [24] developed an entropy-stable scheme on non-conforming affine grids using tensor-product operators that satisfy the SBP property.

In [25] and [26], Hicken, Del Rey Fernández, and Zingg designed a versatile framework to construct multidimensional SBP operators on general elements, such as simplices. In this paper, we utilize this framework to achieve the primary objective of this work, which is to develop high-order, element-wise conservative multidimensional SBP discretizations of the Euler equations applicable to non-conforming grids arising from h-adaptivity, p-adaptivity, and hp-adaptivity. More specifically, we present three methods. The first scheme is based on energy analysis and builds on previous work with tensor-product SBP operators (see the work of Friedrich et al. [27] and the references therein). The second scheme is an extension of the non-conforming entropy-stable tensor-product scheme of [24] to multidimensional SBP operators with collocated volume cubature and facet quadrature nodes, which are analogous to the collocated discontinuous Galerkin (DG) operators constructed on the Legendre-Gauss-Lobatto (LGL) nodes. The third and final scheme is a generalization of the second and is compatible with SBP operators without collocated volume and facet nodes, such as the DG operators constructed on the Legendre-Gauss (LG) nodes. This scheme can be viewed as an extension of the conforming entropy-stable method developed by Crean et al. [14] to non-conforming affine grids. The final objective of this paper is to investigate the advantages of each scheme by performing numerical studies comparing all three methods in terms of efficiency and robustness.

This paper is organized as follows. Section II introduces the notation that is used throughout this paper. In Section III, we present the multidimensional SBP operators and interface interpolation and projection operators for non-conforming facets; we also provide a brief review on entropy stability. The schemes are introduced in Section IV. Section V provides numerical results demonstrating the design-order accuracy, element-wise conservation, and stability properties of the schemes. It also contains a study comparing the methods in terms of computational efficiency and robustness. Our final remarks, including ongoing work, are presented in Section VI.

II. Notation

This section introduces the notation used throughout the paper, which is consistent with the second author's previous papers (e.g. [14, 26]).

To apply the two-dimensional version of the discrete schemes presented in this work, we first triangulate the two-dimensional domain $\Omega \subset \mathbb{R}^2$ into n_e non-overlapping elements, i.e.

$$\mathcal{T}_h \equiv \left\{ \{\Omega_\kappa\}_{\kappa=1}^{n_e} \mid \Omega = \cup_{\kappa=1}^{n_e} \overline{\Omega}_\kappa,\ \Omega_\kappa \cap \Omega_\tau = \emptyset, \kappa \neq \tau \right\},$$

where we consider $\overline{\Omega}_\kappa \equiv \Omega_\kappa \cup \partial\Omega_\kappa$ as the closure of the open element Ω_κ. The set of all facets of the triangulation $\mathcal{T}_h$ is denoted as $\Gamma_h \equiv \{\gamma\}$, which can be divided into a boundary facet set $\Gamma_{h,b} \equiv \{\gamma \in \Gamma_h \mid \gamma \cap \partial\Omega \neq \emptyset\}$ and an interior facet set $\Gamma_{h,i} \equiv \{\Gamma_h \setminus \Gamma_{h,b}\}$. Each $\gamma \in \Gamma_{h,i}$ borders two elements. In this paper, these are referred to as neighbouring elements. Furthermore, the notation $\sum_{\kappa\gamma} \cdot$ is used to indicate a sum over all the facets of element κ, i.e. $\Gamma_h^{(\kappa)} \equiv \{\gamma \in \partial\Omega_\kappa\}$.

Script type upper case letters are reserved for continuous functions and bold type indicates vector-valued functions. For instance, $\mathcal{S}(x,y) \in L^2(\Omega)$ and $\boldsymbol{\mathcal{U}}(x,y) \in [L^2(\Omega)]^4$ are square-integrable scalar and 4-vector-valued functions, respectively, in Ω. The restriction of continuous functions on the nodes of an element is denoted using lower case bold type. For instance, the restriction of $\boldsymbol{\mathcal{U}}(x,y)$ on the set of nodes $S_\kappa \equiv \{(x_i,y_i)\}_{i=1}^{N_\kappa}$ of element κ is $\boldsymbol{u}_\kappa \in \mathbb{R}^{4\cdot N_\kappa}$ where the values of $\boldsymbol{\mathcal{U}}$ at the first node run first, followed by the second node's values, etc. In other words,

$$\boldsymbol{u}_\kappa = \left[\boldsymbol{\mathcal{U}}(x_1,y_1)^\top \quad \cdots \quad \boldsymbol{\mathcal{U}}(x_{N_\kappa},y_{N_\kappa})^\top\right]^\top, \quad \text{where}$$

$$\boldsymbol{\mathcal{U}}(x,y) = \left[\boldsymbol{\mathcal{U}}^{(1)}(x,y) \quad \cdots \quad \boldsymbol{\mathcal{U}}^{(4)}(x,y)\right]^\top.$$

To define the discretization operators in Section III.A, we will use $\mathcal{P}$ and $\mathcal{Q} \in \mathbb{P}_p$ which span the polynomial space of degree p. Their restriction on a set of nodes is denoted by $\boldsymbol{p}$ and $\boldsymbol{q}$, respectively. The symbols $\mathbf{1}$ and $\mathbf{0}$ are reserved for column-vectors consisting of all ones and zeros, respectively (their size can be inferred from the context). Sans-serif upper case letters denote matrices, e.g. $\mathsf{X} \in \mathbb{R}^{n\times m}$, with $\mathsf{I}_n \in \mathbb{R}^{n\times n}$ reserved for the $n \times n$ identity matrix. Finally, the symbol $\circ$ is used to represent the Hadamard (or element-wise) product, whereas $\otimes$ is used to represent the Kronecker product.

III. Preliminaries

A. Multidimensional Summation-by-Parts Operators

For conciseness, the spatial discretization operators presented in this section are for two-dimensional reference elements; however, the extension to three-dimensional reference elements is straightforward. The discrete derivative and integration operators used in this paper, first introduced in [25, 26], are applicable on general elements and satisfy the SBP property.

Definition 1 *Multidimensional summation-by-parts operators. The operator* $\hat{\mathsf{D}}_\xi \in \mathbb{R}^{N\times N}$ *of degree* p *is said to be a summation-by-parts approximation of the first-derivative* $\frac{\partial}{\partial\xi}$ *on the set of nodes* $S \equiv \{(\xi_i, \eta_i)\}_{i=1}^N$ *of a reference element with domain* $\hat{\Omega} \in \mathbb{R}^2$*, if it satisfies the following conditions:*

1) $[\hat{\mathsf{D}}_\xi \boldsymbol{p}]_i = \frac{\partial \mathcal{P}}{\partial \xi}(\xi_i, \eta_i)\ \forall\ \mathcal{P} \in \mathbb{P}_p(\hat{\Omega})$ *and* $i = 1, ..., N$*;*

2) $\hat{\mathsf{D}}_\xi = \hat{\mathsf{H}}^{-1}\hat{\mathsf{Q}}_\xi$*, where* $\hat{\mathsf{H}} = \hat{\mathsf{H}}^\top$*, and* $\boldsymbol{x}^\top \hat{\mathsf{H}} \boldsymbol{x} > 0\ \forall\ \boldsymbol{x} \neq \mathbf{0}$*; and*

3) $\hat{\mathsf{Q}}_\xi + \hat{\mathsf{Q}}_\xi^\top = \hat{\mathsf{E}}_\xi$*; and* $\boldsymbol{q}^\top \hat{\mathsf{E}}_\xi \boldsymbol{p} = \int_{\partial\hat{\Omega}} \mathcal{P}\mathcal{Q} n_\xi \, \mathrm{d}\Gamma\ \forall\ \mathcal{P}, \mathcal{Q} \in \mathbb{P}_{r\geq p}(\hat{\Omega})$*,*

where n_ξ *is the component of the outward pointing normal unit vector in the* ξ*-direction. The operators* $\hat{\mathsf{D}}_\eta$*,* $\hat{\mathsf{Q}}_\eta$*, and* $\hat{\mathsf{E}}_\eta$ *for the* η*-direction are defined similarly.*

The symbol $\hat{}$ serves to emphasize the fact that the SBP operators are constructed on a reference element. The physical operators in the xy-coordinate system can be constructed from the reference element operators in the $\xi\eta$-coordinate system using a geometric mapping function. In this work, we focus on affinely mapped elements. The first condition is known as the accuracy condition and ensures that the derivative operator $\hat{\mathsf{D}}_\xi \in \mathbb{R}^{N\times N}$ accurately approximates first-order derivative terms to a prescribed degree. The matrix $\hat{\mathsf{H}} \in \mathbb{R}^{N\times N}$, known as the norm matrix (or as the mass matrix in the finite-element community), is a symmetric, positive-definite operator. In this paper, only diagonal-norm SBP operators are considered. The entries of the diagonal-norm matrix, along with the set of nodal coordinates S, form a degree $q \geq 2p-1$ cubature rule. Condition 3 requires that the symmetric matrix $\hat{\mathsf{E}}_\xi \in \mathbb{R}^{N\times N}$ be a discrete operator which approximates surface integrals in the ξ-direction. Finally, combining all the conditions, it can be shown that the SBP operators discretely mimic integration-by-parts. In the continuous case, the mathematical representation of integration-by-parts is

$$\int_{\hat{\Omega}} \mathcal{V}\frac{\partial \mathcal{U}}{\partial \xi}\,\mathrm{d}\Omega + \int_{\hat{\Omega}} \frac{\partial \mathcal{V}}{\partial \xi}\mathcal{U}\,\mathrm{d}\Omega = \int_{\partial\hat{\Omega}} \mathcal{V}\mathcal{U} n_\xi \,\mathrm{d}\Gamma. \tag{1}$$

The discrete analogue, i.e. summation-by-parts, is satisfied by the SBP operators:

$$\boldsymbol{v}^\top \hat{\mathsf{Q}}_\xi \boldsymbol{u} + \boldsymbol{v}^\top \hat{\mathsf{Q}}_\xi^\top \boldsymbol{u} = \boldsymbol{v}^\top \hat{\mathsf{E}}_\xi \boldsymbol{u}, \quad \forall\ \boldsymbol{v}, \boldsymbol{u} \in \mathbb{R}^N. \tag{2}$$

Note that there is a one-to-one correspondence between the terms of equations (1) and (2) (e.g. $\boldsymbol{v}^\top \hat{\mathsf{E}}_\xi \boldsymbol{u} \approx \int_{\partial\hat{\Omega}} \mathcal{V}\mathcal{U} n_\xi \,\mathrm{d}\Gamma$). The SBP property (2) is essential for the element-wise conservation and stability properties of the schemes presented in this report.

To construct $\hat{\mathsf{E}}_\xi$, we follow the approach outlined in [26]. We first decompose $\hat{\mathsf{E}}_\xi$ into separate operators for each of the n_f linear and non-overlapping facets $\hat{\gamma}$ of the reference element with nodal set $S_\gamma \equiv \{(\xi_l^{(\gamma)}, \eta_l^{(\gamma)})\}_{l=1}^{N_\gamma}$. We then further decompose these individual operators into an interpolation operator $\mathsf{R}_\gamma \in \mathbb{R}^{N_\gamma \times N}$, a diagonal facet mass matrix $\hat{\mathsf{B}}_\gamma \in \mathbb{R}^{N_\gamma \times N_\gamma}$, and a diagonal matrix $\hat{\mathsf{N}}_{\gamma,\xi} \in \mathbb{R}^{N_\gamma \times N_\gamma}$, which holds the ξ-direction component of the normal unit vector. We can express these decompositions mathematically as

$$\hat{\mathsf{E}}_\xi \equiv \sum_{\hat{\gamma}\in\partial\hat{\Omega}} \hat{\mathsf{E}}_\xi^\gamma = \sum_{\hat{\gamma}\in\partial\hat{\Omega}} \mathsf{R}_\gamma^\top \hat{\mathsf{N}}_{\gamma,\xi} \hat{\mathsf{B}}_\gamma \mathsf{R}_\gamma. \tag{3}$$

A similar decomposition holds for $\hat{\mathsf{E}}_\eta$. Note that since the reference element has piecewise linear facets, the normal unit vector is constant along each facet, e.g. $\hat{\mathsf{N}}_{\gamma,\xi} = n_\xi \mathsf{I}_{N_\gamma}$. In order to satisfy condition 3 of Definition 1, we require an interpolation operator that exactly interpolates polynomials of at least degree $r \geq p$ from the volume to the facet nodes and a facet quadrature rule which exactly integrates polynomials of at least degree $s \geq 2r$, i.e.

$$[\mathsf{R}_\gamma \boldsymbol{p}]_l = [\boldsymbol{p}_\gamma]_l = \mathcal{P}(\xi_l^{(\gamma)}, \eta_l^{(\gamma)})\ \forall\ \mathcal{P} \in \mathbb{P}_{r\geq p}(\hat{\Omega}) \text{ and } l = 1, ..., N_\gamma,$$

and

$$\mathbf{1}^\top \hat{\mathsf{B}}_\gamma \boldsymbol{p}_\gamma = \int_{\partial\hat{\Omega}_\gamma} \mathcal{P}\,\mathrm{d}\Gamma\ \forall\ \mathcal{P} \in \mathbb{P}_{s\geq 2r}(\partial\hat{\Omega}_\gamma).$$

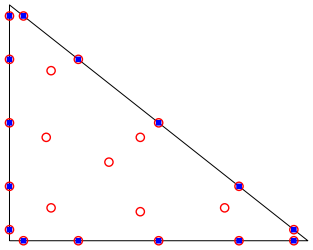

Fig. 1 Diagonal-E $p = 4$ SBP operator with 22 cubature volume nodes (○) and LG quadrature facet nodes (■) [13].

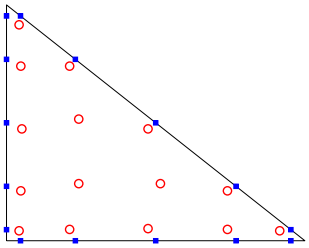

Fig. 2 Ω $p = 4$ SBP operator with 15 cubature volume nodes (○) and LG quadrature facet nodes (■) [26].

Remark 1 *The tensor-product SBP operators can also be defined using the multidimensional SBP notation as shown in, for instance, [27].*

Remark 2 *We note that an $s \geq 2p$ facet quadrature rule is sufficient but not necessary to satisfy the SBP property. In fact, all classical SBP operators and the tensor-product DG operators constructed on the LGL nodes satisfy the SBP property although they are equipped with a degree $2p - 1$ quadrature rule. This induces suboptimal convergence rates for non-conforming schemes using these tensor-product SBP operators. This is further discussed in Section III.B.*

SBP operators which have collocated volume cubature and facet quadrature nodes, as illustrated in Figure 1, have certain beneficial properties*. For this subset of SBP operators, the interpolation operator R_γ reduces to the Kronecker delta, i.e. $[\mathsf{R}_\gamma]_{li} = \delta_{li}\ \forall i = 1, ..., N$ and $l = 1, ..., N_\gamma$, and the operator simply "picks" the volume cubature nodes that collocate with the facet quadrature nodes instead of performing an interpolation. Furthermore, the surface integration operator E_ξ is diagonal (we thus refer to this subset of SBP operators as diagonal-E SBP operators). The Kronecker delta structure of R_γ and the diagonal structure of E_ξ are often invoked in conservation and stability proofs, for instance, by commuting the E_ξ matrix with another diagonal matrix. Furthermore, since both R_γ and E_ξ are sparse matrices, surface integrals can be computed in an efficient manner. These operators on simplices, however, have more volume nodes than the minimum number needed for a degree p operator. Consequently, the computation of volume terms is generally more expensive for these operators than for the Ω SBP operators, which have minimal or nearly minimal numbers of volume nodes (see Figure 2). Nevertheless, when considering the total cost of the spatial discretization scheme, diagonal-E operators, such as the LGL operators, could be computationally less expensive than dense-E operators for entropy-stable methods (see Refs. [14, 17, 28]). On the other hand, the Ω operators are generally more accurate than the diagonal-E operators for a given degree p. In this paper, we perform a numerical investigation in order to compare the efficiency of diagonal-E and dense-E entropy-stable schemes on non-conforming grids.

B. Interface Interpolation and Projection Operators

1. p-adaptivity

The coupling of two neighbouring elements κ and ν with a shared conforming facet γ (i.e. no hanging nodes) and conforming facet nodal distribution (i.e. same degree p) can be performed relatively easily. To be more precise, since both elements share the same facet nodes, as shown in Figure 3, the numerical fluxes can be evaluated in a point-wise manner. In the case of a conforming interface of two different degree operators (e.g. degree $p + 1$ on κ and p on ν), the interface nodal distribution is non-conforming, as illustrated in Figure 4. In such a case, the coupling of the two elements is more complex and must be handled with care. The first and third schemes introduced in Section IV perform interface couplings on an intermediate interface (also known as a mortar element), whereas the second scheme does not directly use intermediate interfaces. In this section, we present the interface interpolation and projection operators that are used by these schemes and the conditions that they must satisfy such that the accuracy, element-wise conservation, and stability properties of the discretizations hold.

When the interface coupling is performed on the intermediate interface, we utilize the operator $\mathsf{P}_{\kappa\gamma\to I} \in \mathbb{R}^{N_I \times N_{\kappa\gamma}}$ to interpolate values from the nodes of facet γ of element κ onto the intermediate interface's nodes represented

*These are analogous to one-dimensional operators with boundary nodes.

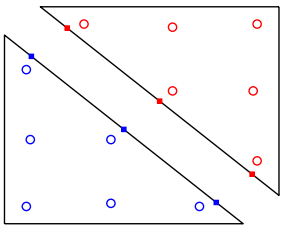

Fig. 3 Two Ω $p = 2$ elements with conforming interface nodal distributions. An intermediate interface is not required.

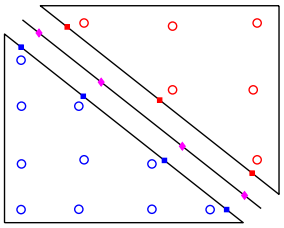

Fig. 4 An Ω $p = 3$ element coupled with an Ω $p = 2$ element using an intermediate interface.

by I. Similarly, the operator $\mathsf{P}_{\nu\gamma\to I} \in \mathbb{R}^{N_I \times N_{\nu\gamma}}$ interpolates values from the facet nodes of element ν onto the intermediate interface's nodes. Letting $S_I \equiv \{(x_k^{(I)}, y_k^{(I)})\}_{k=1}^{N_I}$ be the nodal set associated with the intermediate interface's quadrature rule, these operators need to satisfy the following conditions:

1) $[\mathsf{P}_{\kappa\gamma\to I}\boldsymbol{q}_{\kappa\gamma}]_k = \mathcal{Q}(x_k^{(I)}, y_k^{(I)})\ \forall \mathcal{Q} \in \mathbb{P}_{r_\kappa}(\partial\Omega_\gamma)$ and $k = 1, ..., N_I$,
   $[\mathsf{P}_{\nu\gamma\to I}\boldsymbol{q}_{\nu\gamma}]_k = \mathcal{Q}(x_k^{(I)}, y_k^{(I)})\ \forall \mathcal{Q} \in \mathbb{P}_{r_\nu}(\partial\Omega_\gamma)$ and $k = 1, ..., N_I$,
2) $\mathsf{R}_{\kappa\gamma}^\top \mathsf{B}_{\kappa\gamma}\mathsf{R}_{\kappa\gamma} = \mathsf{R}_{\kappa\gamma}^\top \mathsf{P}_{\kappa\gamma\to I}^\top \mathsf{B}_I \mathsf{P}_{\kappa\gamma\to I}\mathsf{R}_{\kappa\gamma}$,
   $\mathsf{R}_{\nu\gamma}^\top \mathsf{B}_{\nu\gamma}\mathsf{R}_{\nu\gamma} = \mathsf{R}_{\nu\gamma}^\top \mathsf{P}_{\nu\gamma\to I}^\top \mathsf{B}_I \mathsf{P}_{\nu\gamma\to I}\mathsf{R}_{\nu\gamma}$,

where $\boldsymbol{q}_{\kappa\gamma}$ and $\boldsymbol{q}_{\nu\gamma}$ are the values of polynomial $\mathcal{Q}$ evaluated at the nodal set of $\kappa\gamma$, $S_{\kappa\gamma} \equiv \{(x_l^{(\kappa\gamma)}, y_l^{(\kappa\gamma)})\}_{l=1}^{N_{\kappa\gamma}}$, and $\nu\gamma$, $S_{\nu\gamma} \equiv \{(x_m^{(\nu\gamma)}, y_m^{(\nu\gamma)})\}_{m=1}^{N_{\nu\gamma}}$, respectively, and $\mathsf{B}_I \in \mathbb{R}^{N_I \times N_I}$ is the diagonal facet mass matrix of the intermediate interface. The first is the accuracy condition of the interface interpolation operators, and the second preserves the SBP property without modifying the volume operators Q_x, Q_y, E_x, E_y, D_x, and D_y on affine grids. The proof that such interpolation operators exist requires the facet mass matrices $\mathsf{B}_{\kappa\gamma}$ and $\mathsf{B}_{\nu\gamma}$ to be of degree $s_\kappa \geq 2r_\kappa \geq 2p_\kappa$ and $s_\nu \geq 2r_\nu \geq 2p_\nu$, respectively, and the intermediate interface's mass matrix B_I to be of degree $s_I \geq \max(s_\kappa, s_\nu)$. This proof will be presented in a future paper.

Remark 3 *In this work, the intermediate interface's quadrature rule is chosen as the more accurate quadrature rule of the two neighbouring elements for computational efficiency. For instance, if $s_\kappa > s_\nu$, $S_I \equiv S_{\kappa\gamma}$ and $\mathsf{B}_I \equiv \mathsf{B}_{\kappa\gamma}$.*

For the second scheme, which does not directly use an intermediate interface to couple non-conforming interfaces, we utilize the operator $\mathsf{P}_{\nu\gamma\to\kappa\gamma} \in \mathbb{R}^{N_{\kappa\gamma} \times N_{\nu\gamma}}$ which projects values from the facet nodes of element ν onto the facet nodes of element κ ($\mathsf{P}_{\kappa\gamma\to\nu\gamma} \in \mathbb{R}^{N_{\nu\gamma} \times N_{\kappa\gamma}}$ performs the inverse task). Similar to [24], we require that these operators satisfy

$$\mathsf{P}_{\kappa\gamma\to\nu\gamma}^\top \mathsf{B}_{\nu\gamma} = \mathsf{B}_{\kappa\gamma}\mathsf{P}_{\nu\gamma\to\kappa\gamma}$$

for element-wise conservation and entropy-conservation. Since the facet mass matrices are diagonal by construction, we can rewrite the equation in index notation as

$$[\mathsf{P}_{\kappa\gamma\to\nu\gamma}]_{ml}[\mathsf{B}_{\nu\gamma}]_{mm} = [\mathsf{B}_{\kappa\gamma}]_{ll}[\mathsf{P}_{\nu\gamma\to\kappa\gamma}]_{lm}\ \forall l = 1, ..., N_{\kappa\gamma},\ \text{and}\ m = 1, ..., N_{\nu\gamma}.$$

This condition ensures that the following discrete inner product holds

$$(\mathsf{P}_{\kappa\gamma\to\nu\gamma}\boldsymbol{v}_{\kappa\gamma})^\top \mathsf{B}_{\nu\gamma}\boldsymbol{u}_{\nu\gamma} = \boldsymbol{v}_{\kappa\gamma}\mathsf{B}_{\kappa\gamma}(\mathsf{P}_{\nu\gamma\to\kappa\gamma}\boldsymbol{u}_{\nu\gamma}), \quad \forall \boldsymbol{v}_{\kappa\gamma} \in \mathbb{R}^{N_{\kappa\gamma}} \text{ and } \boldsymbol{u}_{\nu\gamma} \in \mathbb{R}^{N_{\nu\gamma}}.$$

Remark 4 *The interface projection process can be conceptually divided into two steps: values are first interpolated from an element's facet nodes to the intermediate interface's nodes; these are then projected onto the neighbouring element's facet nodes. Mathematically, this is equivalent to $\mathsf{P}_{\nu\gamma\to\kappa\gamma} = \mathsf{P}_{I\to\kappa\gamma}\mathsf{P}_{\nu\gamma\to I}$ and $\mathsf{P}_{\kappa\gamma\to\nu\gamma} = \mathsf{P}_{I\to\nu\gamma}\mathsf{P}_{\kappa\gamma\to I}$.*

Appendix A provides a detailed outline for the construction of the interface's interpolation and projection operators. In the DG and the SBP communities, the tensor-product LGL operators with $2p - 1$ accurate quadrature rules are often used in conforming energy-stable and entropy-stable schemes (see, for instance, [12, 29]). These operators have collocated volume and facet nodes (i.e. they are diagonal-E SBP operators), which is a desired property for entropy-stable

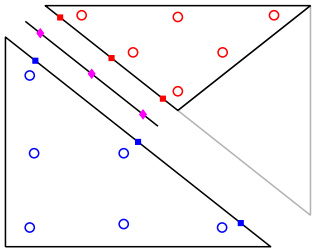

Fig. 5 The coupling of elements with a hanging node.

schemes as previously mentioned. Unfortunately, for non-conforming schemes, LGL operators induce suboptimal convergence rates, as numerically shown in [24, 27, 30]. The underlying reason is that interface projection operators of degree p cannot be constructed for SBP operators with facet quadrature rules of degree less than $2p$. In order to avoid this reduction in convergence, we utilize diagonal-E SBP operators with facet quadrature rules of degree $s \geq 2r \geq 2p$. We thus require that the projection operators satisfy the following accuracy constraint

$$[\mathsf{P}_{\nu\gamma\to\kappa\gamma}\boldsymbol{q}_{\nu\gamma}]_l = \mathcal{Q}(x_l^{(\kappa\gamma)}, y_l^{(\kappa\gamma)})\ \forall \mathcal{Q} \in \mathbb{P}_{r_{\min}}(\partial\Omega_\gamma) \text{ and } l = 1, ..., N_{\kappa\gamma},$$
$$[\mathsf{P}_{\kappa\gamma\to\nu\gamma}\boldsymbol{q}_{\kappa\gamma}]_m = \mathcal{Q}(x_m^{(\nu\gamma)}, y_m^{(\nu\gamma)})\ \forall \mathcal{Q} \in \mathbb{P}_{r_{\min}}(\partial\Omega_\gamma) \text{ and } m = 1, ..., N_{\nu\gamma},$$

where $r_{\min} \equiv \min(r_\kappa, r_\nu)$.

2. h-adaptivity and hp-adaptivity

In the case of neighbouring elements of constant degree with hanging nodes (i.e. h-adaptivity), the largest element's facet is divided into subfacets which conform with the smaller elements' facets, as shown in Figure 5. Since the largest element's original facet's nodal distribution is non-conforming with the interface's nodal distribution, the approach outlined in Section III.B.1 is then followed to compute the interface interpolation and projection operators. In the case of neighbouring elements of different degrees with hanging nodes (i.e. hp-adaptivity), the same approach as h-adaptivity is taken.

C. Euler Equations

For conciseness, the schemes presented in Section IV are for the two-dimensional Euler equations. It is worth noting that the entropy-stable schemes are applicable to any system of hyperbolic conservation laws (of any dimension) endowed with an entropy pair. The two-dimensional Euler equations in conservative form are

$$\frac{\partial \boldsymbol{\mathcal{U}}}{\partial t} + \frac{\partial \boldsymbol{\mathcal{F}}_x}{\partial x} + \frac{\partial \boldsymbol{\mathcal{F}}_y}{\partial y} = \mathbf{0},\ (x, y) \in \Omega \in \mathbb{R}^2, t \geq 0, \tag{4}$$

with

$$\boldsymbol{\mathcal{U}} = \begin{bmatrix} \rho \\ \rho u \\ \rho v \\ e \end{bmatrix},\ \boldsymbol{\mathcal{F}}_x = \begin{bmatrix} \rho u \\ \rho u^2 + p \\ \rho uv \\ \rho uh \end{bmatrix},\ \text{and } \boldsymbol{\mathcal{F}}_y = \begin{bmatrix} \rho v \\ \rho uv \\ \rho v^2 + p \\ \rho vh \end{bmatrix},$$

where ρ is the density, u and v are the velocity components in the x- and y-directions respectively, e is the total energy per unit volume, p is the pressure, and $h \equiv \frac{e+p}{\rho}$ is the total enthalpy per unit mass of the fluid. Assuming the calorically perfect gas assumption applies,

$$p = (\gamma - 1)(e - \rho\frac{u^2 + v^2}{2}),$$

where γ is the heat capacity ratio ($\gamma = 1.4$ for air).

D. The Importance of the Entropy Inequality

The satisfaction of a mathematical entropy inequality has many benefits[†]. First, Friedrichs and Lax [31] proved through the use of a vanishing viscosity mechanism that solutions satisfying an entropy inequality

$$\frac{\partial \mathcal{S}}{\partial t} + \frac{\partial \mathcal{G}_x}{\partial x} + \frac{\partial \mathcal{G}_y}{\partial y} \leq 0, \tag{5}$$

where $\mathcal{S}$ is the mathematical entropy and $\mathcal{G}_x$ and $\mathcal{G}_y$ are the entropy fluxes in the x- and y-directions respectively, are the physically relevant solutions. For solutions with discontinuities, this is important since weak solutions are not unique. In addition to singling out the physically relevant solution, the satisfaction of the entropy inequality can provide a sufficient condition for nonlinear stability (known as entropy stability) as shown by Dafermos [32] and Svärd [33]. To be more precise, a bound on the entropy ensures an L^2 bound on the solution $\boldsymbol{\mathcal{U}}$ of the Navier-Stokes equations given that temperature and density are positive.

The Euler equations (4) are said to be endowed with an entropy-entropy-flux pair ($\mathcal{S}$, $\mathcal{G}$) since the following conditions are satisfied:

$$\left(\frac{\partial^2 \mathcal{S}}{\partial \boldsymbol{\mathcal{U}}^2}\right) = \left(\frac{\partial^2 \mathcal{S}}{\partial \boldsymbol{\mathcal{U}}^2}\right)^\top, \quad \boldsymbol{x}^\top \frac{\partial^2 \mathcal{S}}{\partial \boldsymbol{\mathcal{U}}^2} \boldsymbol{x} > 0, \boldsymbol{x} \neq \boldsymbol{0}, \tag{6a}$$

$$\frac{\partial \mathcal{G}_x}{\partial \boldsymbol{\mathcal{U}}} = \frac{\partial \mathcal{S}}{\partial \boldsymbol{\mathcal{U}}} \frac{\partial \boldsymbol{\mathcal{F}}_x}{\partial \boldsymbol{\mathcal{U}}}, \quad \text{and} \quad \frac{\partial \mathcal{G}_y}{\partial \boldsymbol{\mathcal{U}}} = \frac{\partial \mathcal{S}}{\partial \boldsymbol{\mathcal{U}}} \frac{\partial \boldsymbol{\mathcal{F}}_y}{\partial \boldsymbol{\mathcal{U}}}, \tag{6b}$$

for $\mathcal{S} \equiv -\rho s/(\gamma - 1)$, $\mathcal{G}_x \equiv u\mathcal{S}$, and $\mathcal{G}_y \equiv v\mathcal{S}$, where $s \equiv \ln(\frac{p}{\rho^\gamma})$ is the thermodynamic entropy per unit mass. Furthermore, since the Hessian of the entropy is symmetric positive-definite, there exists a one-to-one mapping between the conservative and entropy variables $\boldsymbol{\mathcal{W}} \equiv \frac{\partial \mathcal{S}}{\partial \boldsymbol{\mathcal{U}}} \in \mathbb{R}^4$ where

$$\boldsymbol{\mathcal{W}} = \left[\tfrac{\gamma - s}{\gamma - 1} - \tfrac{\rho}{2p}(u^2 + v^2), \tfrac{\rho u}{p}, \tfrac{\rho v}{p}, -\tfrac{\rho}{p}\right]^\top.$$

When the governing equations are written in terms of the entropy variables, they form a well-posed symmetric hyperbolic system of equations [31, 34, 35], i.e. the matrices $\frac{\partial \boldsymbol{\mathcal{F}}_x}{\partial \boldsymbol{\mathcal{W}}}$ and $\frac{\partial \boldsymbol{\mathcal{F}}_y}{\partial \boldsymbol{\mathcal{W}}}$ in

$$\frac{\partial \boldsymbol{\mathcal{U}}}{\partial \boldsymbol{\mathcal{W}}} \frac{\partial \boldsymbol{\mathcal{W}}}{\partial t} + \frac{\partial \boldsymbol{\mathcal{F}}_x}{\partial \boldsymbol{\mathcal{W}}} \frac{\partial \boldsymbol{\mathcal{W}}}{\partial x} + \frac{\partial \boldsymbol{\mathcal{F}}_y}{\partial \boldsymbol{\mathcal{W}}} \frac{\partial \boldsymbol{\mathcal{W}}}{\partial y} = \boldsymbol{0},$$

are symmetric and $\frac{\partial \boldsymbol{\mathcal{U}}}{\partial \boldsymbol{\mathcal{W}}}$ is symmetric postive-definite[‡].

E. Discrete Entropy Conservation

To derive the equality portion of the entropy inequality (5) at the continuous level, we left-multiply the Euler equations (4) by the entropy variables and simplify as follows

$$\begin{aligned}
\boldsymbol{\mathcal{W}}^\top \left(\frac{\partial \boldsymbol{\mathcal{U}}}{\partial t} + \frac{\partial \boldsymbol{\mathcal{F}}_x}{\partial x} + \frac{\partial \boldsymbol{\mathcal{F}}_y}{\partial y}\right) &= 0, \\
\frac{\partial \mathcal{S}}{\partial \boldsymbol{\mathcal{U}}} \cdot \frac{\partial \boldsymbol{\mathcal{U}}}{\partial t} + \frac{\partial \mathcal{S}}{\partial \boldsymbol{\mathcal{U}}} \frac{\partial \boldsymbol{\mathcal{F}}_x}{\partial \boldsymbol{\mathcal{U}}} \frac{\partial \boldsymbol{\mathcal{U}}}{\partial x} + \frac{\partial \mathcal{S}}{\partial \boldsymbol{\mathcal{U}}} \frac{\partial \boldsymbol{\mathcal{F}}_y}{\partial \boldsymbol{\mathcal{U}}} \frac{\partial \boldsymbol{\mathcal{U}}}{\partial y} &= 0, \\
\frac{\partial \mathcal{S}}{\partial t} + \frac{\partial \mathcal{G}_x}{\partial x} + \frac{\partial \mathcal{G}_y}{\partial y} &= 0,
\end{aligned}$$

where we used the chain rule and the contraction property (6b). Note that the equality only holds for smooth solutions; for discontinuous solutions, we must use the vanishing viscosity mechanism of [31] and equation (6a) to show that the mathematical entropy is non-increasing. Although the chain rule holds at the continuous level, it generally does not hold

[†]For the gas dynamics equations, the mathematical entropy inequality is the second law of thermodynamics with one minor difference: whereas the thermodynamic entropy is non-decreasing, the mathematical entropy is non-increasing.

[‡]Although there exist many choices of entropy $\mathcal{S}$ that symmetrize the Euler equations, the one presented in this paper is the only one that also symmetrizes the viscous fluxes of the Navier-Stokes equations [9].

when the derivative of the flux is discretely approximated. In 1987, Tadmor [36] derived a condition which allows the equality portion of the entropy inequality to be satisfied at the discrete level even when the chain rule does not hold. Tadmor's condition is defined as

$$\left(\boldsymbol{\mathcal{W}}(\boldsymbol{\mathcal{U}}_1) - \boldsymbol{\mathcal{W}}(\boldsymbol{\mathcal{U}}_2)\right)^\top \boldsymbol{\mathcal{F}}_x^{*,\mathrm{EC}}(\boldsymbol{\mathcal{U}}_1, \boldsymbol{\mathcal{U}}_2) = \psi_x(\boldsymbol{\mathcal{U}}_1) - \psi_x(\boldsymbol{\mathcal{U}}_2), \tag{7}$$

where the subscripts 1 and 2 indicate two different states, and $\psi_x \equiv \boldsymbol{\mathcal{W}}^\top \boldsymbol{\mathcal{F}}_x - \mathcal{G}_x$ is known as the potential flux in the x-direction. For the Euler equations, $\psi_x = \rho u$. A similar condition exists for the y-direction. We term any numerical flux satisfying Tadmor's condition as entropy-conservative (EC). These fluxes are a key component of entropy-conservative and entropy-stable schemes.

Remark 5 *Note that (7) is a single equation whereas the numerical flux is a vector for systems of equations. Therefore, entropy-conservative fluxes are not unique. In fact, for the Euler equations, there exist multiple entropy-conservative fluxes such as Tadmor's [36], Ismail and Roe's [11], Chandrashekar's [37], and Ranocha's [38]. In addition to satisfying Tadmor's condition, these fluxes are also consistent and symmetric in their arguments, i.e.* $\boldsymbol{\mathcal{F}}_x^{*,EC}(\boldsymbol{\mathcal{U}}, \boldsymbol{\mathcal{U}}) = \boldsymbol{\mathcal{F}}_x(\boldsymbol{\mathcal{U}})$ *and* $\boldsymbol{\mathcal{F}}_x^{*,EC}(\boldsymbol{\mathcal{U}}_1, \boldsymbol{\mathcal{U}}_2) = \boldsymbol{\mathcal{F}}_x^{*,EC}(\boldsymbol{\mathcal{U}}_2, \boldsymbol{\mathcal{U}}_1)$.

IV. Non-Conforming Semi-Discrete Schemes

In this section, we present three non-conforming, high-order semi-discrete schemes applicable on general elements. The first, termed the "energy-stable scheme", is provably stable for linear differential equations and builds on the work of [27] and the references therein. An extension of the tensor-product discretization scheme presented in [24], the second is entropy-conservative and is only compatible with diagonal-E SBP operators, as it relies on the collocation structure of the volume and facet nodes of these operators. Accordingly, we term this method the "diagonal-E entropy-conservative scheme". The third method, referred to as the "dense-E entropy-conservative scheme", is a generalization of the second method since it is compatible with all diagonal-norm SBP operators. As previously mentioned, the third scheme can also be seen as an extension of Crean et al.'s scheme [14] to non-conforming grids. Furthermore, an entropy dissipative interface stabilization term can be added to the entropy-conservative schemes to make them entropy-stable. All three methods are element-wise conservative and design-order accurate. The accuracy, conservation, and stability proofs will be covered in a future paper. Here, these properties are demonstrated through numerical experiments.

A. Energy-stable Scheme

Compared to the entropy-stable schemes presented later in this section, the following scheme is computationally more efficient, but it is not nonlinearly stable. The strong form of the energy-stable scheme, which is compatible with dense-E SBP operators, is

$$\frac{\mathrm{d}\boldsymbol{u}_\kappa}{\mathrm{d}t} + \tilde{\mathsf{D}}_x \boldsymbol{f}_x(\boldsymbol{u}_\kappa) + \tilde{\mathsf{D}}_y \boldsymbol{f}_y(\boldsymbol{u}_\kappa) = -\tilde{\mathsf{H}}^{-1}\left(\sum_{\kappa\gamma} \tilde{\mathsf{R}}_{\kappa\gamma}^\top \tilde{\mathsf{P}}_{\kappa\gamma\to I}^\top \tilde{\mathsf{B}}_I \boldsymbol{f}_n^*(\boldsymbol{u}_{\kappa I}, \boldsymbol{u}_{\nu I}) - \tilde{\mathsf{E}}_x \boldsymbol{f}_x(\boldsymbol{u}_\kappa) - \tilde{\mathsf{E}}_y \boldsymbol{f}_x(\boldsymbol{u}_\kappa)\right), \tag{8}$$

for an arbitrary element κ, where the interpolated solutions on the intermediate interface, $\boldsymbol{u}_{\kappa I} \in \mathbb{R}^{4 \cdot N_I}$ and $\boldsymbol{u}_{\nu I} \in \mathbb{R}^{4 \cdot N_I}$, are defined as $\boldsymbol{u}_{\kappa I} \equiv \tilde{\mathsf{P}}_{\kappa\gamma\to I} \tilde{\mathsf{R}}_{\kappa\gamma} \boldsymbol{u}_\kappa$ and $\boldsymbol{u}_{\nu I} \equiv \tilde{\mathsf{P}}_{\nu\gamma\to I} \tilde{\mathsf{R}}_{\nu\gamma} \boldsymbol{u}_\nu$, respectively. The tilde notation implies the use of the Kronecker product with the identity matrix. For instance, for the two-dimensional Euler equations, we define $\tilde{\mathsf{D}}_x \equiv \mathsf{D}_x \otimes \mathsf{I}_4$ such that it can simultaneously be applied on the system of four equations without coupling terms of different equations. In this work, we use the commonly known Roe flux [39] computed in the normal direction, i.e. $\boldsymbol{f}_n^*(\cdot,\cdot) = \boldsymbol{f}_n^{*,\mathrm{Roe}}(\cdot,\cdot)$.

B. Diagonal-E Entropy-Conservative Scheme

The strong form of the diagonal-E entropy-conservative scheme is, for an arbitrary element κ,

$$\begin{aligned}\frac{\mathrm{d}\boldsymbol{u}_\kappa}{\mathrm{d}t} + 2\left\{\tilde{\mathsf{D}}_x \circ \mathsf{F}_x^{*,\mathrm{EC}}(\boldsymbol{u}_\kappa, \boldsymbol{u}_\kappa)\right\}\mathbf{1}_\kappa + 2\left\{\tilde{\mathsf{D}}_y \circ \mathsf{F}_y^{*,\mathrm{EC}}(\boldsymbol{u}_\kappa, \boldsymbol{u}_\kappa)\right\}\mathbf{1}_\kappa = \\ - \tilde{\mathsf{H}}^{-1}\sum_{\kappa\gamma}\tilde{\mathsf{R}}_{\kappa\gamma}^\top\tilde{\mathsf{B}}_{\kappa\gamma}\left(\tilde{\mathsf{N}}_{\kappa\gamma,x}\boldsymbol{f}_x^{*,\mathrm{EC,NC}}(\boldsymbol{u}_{\kappa\gamma}, \boldsymbol{u}_{\nu\gamma}) + \tilde{\mathsf{N}}_{\kappa\gamma,y}\boldsymbol{f}_y^{*,\mathrm{EC,NC}}(\boldsymbol{u}_{\kappa\gamma}, \boldsymbol{u}_{\nu\gamma})\right) \\ + \tilde{\mathsf{H}}^{-1}\left(\tilde{\mathsf{E}}_x\boldsymbol{f}_x(\boldsymbol{u}_\kappa) + \tilde{\mathsf{E}}_y\boldsymbol{f}_y(\boldsymbol{u}_\kappa)\right),\end{aligned} \tag{9}$$

where the entropy-conservative matrix term $\mathsf{F}_x^{*,\mathrm{EC}}(\boldsymbol{u}_\kappa, \boldsymbol{u}_\kappa)$ can be deduced from the following definition. The matrix flux function $\mathsf{F}_x^{*,\mathrm{EC}}(\boldsymbol{u}_\kappa, \boldsymbol{u}_\nu) : \mathbb{R}^{4\cdot N_\kappa} \times \mathbb{R}^{4\cdot N_\nu} \to \mathbb{R}^{4\cdot N_\kappa \times 4\cdot N_\nu}$ is defined as [14]

$$\mathsf{F}_x^{*,\mathrm{EC}}(\boldsymbol{u}_\kappa, \boldsymbol{u}_\nu) \equiv \begin{bmatrix} \mathrm{diag}\big[\boldsymbol{f}_x^{*,\mathrm{EC}}([\boldsymbol{u}_\kappa]_1, [\boldsymbol{u}_\nu]_1)\big] & \cdots & \mathrm{diag}\big[\boldsymbol{f}_x^{*,\mathrm{EC}}([\boldsymbol{u}_\kappa]_1, [\boldsymbol{u}_\nu]_{N_\nu})\big] \\ \vdots & \ddots & \vdots \\ \mathrm{diag}\big[\boldsymbol{f}_x^{*,\mathrm{EC}}([\boldsymbol{u}_\kappa]_{N_\kappa}, [\boldsymbol{u}_\nu]_1)\big] & \cdots & \mathrm{diag}\big[\boldsymbol{f}_x^{*,\mathrm{EC}}([\boldsymbol{u}_\kappa]_{N_\kappa}, [\boldsymbol{u}_\nu]_{N_\nu})\big] \end{bmatrix}. \tag{10}$$

The volumetric matrix flux term in the y-direction is defined similarly. The entropy-conservative fluxes $\boldsymbol{f}_x^{*,\mathrm{EC}}(\cdot,\cdot)$ are placed in diagonal matrices such that the fluxes of different components of the system of equations are not coupled. In index notation,

$$2\left[\left\{\tilde{\mathsf{D}}_x \circ \mathsf{F}_x^{*,\mathrm{EC}}(\boldsymbol{u}_\kappa, \boldsymbol{u}_\kappa)\right\}\mathbf{1}_\kappa\right]_i = 2\sum_{j=1}^{N_\kappa}[\mathsf{D}_x]_{ij}\boldsymbol{f}_x^{*,\mathrm{EC}}([\boldsymbol{u}_\kappa]_i, [\boldsymbol{u}_\kappa]_j), \forall i = 1, ..., N_\kappa.$$

In other words, the derivative of the flux evaluated at the i^{th} node of element κ is approximated as a linear combination of two-point entropy-conservative fluxes. In the entropy stability research community, such an approximation was first used by LeFloch et al. [40] and is fundamental in developing schemes that are high order and entropy conservative. Finally, the x-direction numerical fluxes coupling neighbouring elements with non-conforming (NC) facet nodal distributions, i.e. $\boldsymbol{f}_x^{*,\mathrm{EC,NC}}(\boldsymbol{u}_{\kappa\gamma}, \boldsymbol{u}_{\nu\gamma}) : \mathbb{R}^{4\cdot N_{\kappa\gamma}} \times \mathbb{R}^{4\cdot N_{\nu\gamma}} \to \mathbb{R}^{4\cdot N_{\kappa\gamma}}$, is defined as

$$\boldsymbol{f}_x^{*,\mathrm{EC,NC}}(\boldsymbol{u}_{\kappa\gamma}, \boldsymbol{u}_{\nu\gamma}) \equiv \left\{\tilde{\mathsf{P}}_{\nu\gamma\to\kappa\gamma} \circ \mathsf{F}_x^{*,\mathrm{EC}}(\boldsymbol{u}_{\kappa\gamma}, \boldsymbol{u}_{\nu\gamma})\right\}\mathbf{1}_{\nu\gamma}, \tag{11}$$

where the interpolated solutions on each element's facet, $\boldsymbol{u}_{\kappa\gamma} \in \mathbb{R}^{4\cdot N_{\kappa\gamma}}$ and $\boldsymbol{u}_{\nu\gamma} \in \mathbb{R}^{4\cdot N_{\nu\gamma}}$, are defined as $\boldsymbol{u}_{\kappa\gamma} \equiv \tilde{\mathsf{R}}_{\kappa\gamma}\boldsymbol{u}_\kappa$ and $\boldsymbol{u}_{\nu\gamma} \equiv \tilde{\mathsf{R}}_{\nu\gamma}\boldsymbol{u}_\nu$, respectively. $\boldsymbol{f}_y^{*,\mathrm{EC,NC}}(\boldsymbol{u}_{\kappa\gamma}, \boldsymbol{u}_{\nu\gamma})$ is defined similarly. Similar to the volumetric flux term, the flux at each facet node of element κ is a linear combination of two-point entropy-conservative flux functions evaluated at that node and all the facet nodes of the neighbouring element ν, i.e.

$$[\boldsymbol{f}_x^{*,\mathrm{EC,NC}}(\boldsymbol{u}_{\kappa\gamma}, \boldsymbol{u}_{\nu\gamma})]_l = \sum_{m=1}^{N_{\nu\gamma}}[\mathsf{P}_{\nu\gamma\to\kappa\gamma}]_{lm}\boldsymbol{f}_x^{*,\mathrm{EC}}([\boldsymbol{u}_{\kappa\gamma}]_l, [\boldsymbol{u}_{\nu\gamma}]_m)\ \forall l = 1, ..., N_{\kappa\gamma}.$$

Remark 6 *On a conforming mesh, the interface projection operators simplify to the identity matrix, and Fisher and Carpenter's [41] or Chen and Shu's [13] schemes on quadrilateral and simplex grids are recovered, respectively.*

C. Dense-E Entropy-Conservative Scheme

The strong form of the dense-E entropy-conservative scheme is, for an arbitrary element κ,

$$\begin{aligned}\frac{\mathrm{d}\boldsymbol{u}_\kappa}{\mathrm{d}t} + 2\left\{\tilde{\mathsf{D}}_x \circ \mathsf{F}_x^{*,\mathrm{EC}}(\boldsymbol{u}_\kappa, \boldsymbol{u}_\kappa)\right\}\mathbf{1}_\kappa + 2\left\{\tilde{\mathsf{D}}_y \circ \mathsf{F}_y^{*,\mathrm{EC}}(\boldsymbol{u}_\kappa, \boldsymbol{u}_\kappa)\right\}\mathbf{1}_\kappa = \\ - \tilde{\mathsf{H}}^{-1}\sum_{\kappa\gamma}\left\{\left(\tilde{\mathsf{R}}_{\kappa\gamma}^\top\tilde{\mathsf{P}}_{\kappa\gamma\to I}^\top\tilde{\mathsf{B}}_I\tilde{\mathsf{N}}_{I,x}\tilde{\mathsf{P}}_{\nu\gamma\to I}\tilde{\mathsf{R}}_{\nu\gamma}\right) \circ \mathsf{F}_x^{*,\mathrm{EC}}(\boldsymbol{u}_\kappa, \boldsymbol{u}_\nu)\right\}\mathbf{1}_\nu + \tilde{\mathsf{H}}^{-1}\left\{\tilde{\mathsf{E}}_x \circ \mathsf{F}_x^{*,\mathrm{EC}}(\boldsymbol{u}_\kappa, \boldsymbol{u}_\kappa)\right\}\mathbf{1}_\kappa \\ - \tilde{\mathsf{H}}^{-1}\sum_{\kappa\gamma}\left\{\left(\tilde{\mathsf{R}}_{\kappa\gamma}^\top\tilde{\mathsf{P}}_{\kappa\gamma\to I}^\top\tilde{\mathsf{B}}_I\tilde{\mathsf{N}}_{I,y}\tilde{\mathsf{P}}_{\nu\gamma\to I}\tilde{\mathsf{R}}_{\nu\gamma}\right) \circ \mathsf{F}_y^{*,\mathrm{EC}}(\boldsymbol{u}_\kappa, \boldsymbol{u}_\nu)\right\}\mathbf{1}_\nu + \tilde{\mathsf{H}}^{-1}\left\{\tilde{\mathsf{E}}_y \circ \mathsf{F}_y^{*,\mathrm{EC}}(\boldsymbol{u}_\kappa, \boldsymbol{u}_\kappa)\right\}\mathbf{1}_\kappa.\end{aligned} \tag{12}$$

Remark 7 *On a conforming mesh, the interface interpolation operators simplify to the identity matrix and Crean et al.'s scheme [14] is recovered.*

D. Entropy-Stable Interface Stabilization Term

The schemes (9) and (12) are entropy conservative. For discontinuous solutions, the second law of thermodynamics, however, dictates that entropy must be generated. As such, following the steps of [14], we add the following interface entropy dissipative term to the right-hand side of the numerical method (9) and (12)[§]:

$$-\tilde{\mathsf{H}}^{-1}\sum_{\kappa\gamma}\tilde{\mathsf{R}}_{\kappa\gamma}^{\top}\tilde{\mathsf{P}}_{\kappa\gamma\to I}^{\top}\tilde{\mathsf{B}}_I|\Lambda_I(\boldsymbol{u}_{\kappa I},\boldsymbol{u}_{\nu I})|(\tilde{\mathsf{P}}_{\kappa\gamma\to I}\tilde{\mathsf{R}}_{\kappa\gamma}\boldsymbol{w}_\kappa-\tilde{\mathsf{P}}_{\nu\gamma\to I}\tilde{\mathsf{R}}_{\nu\gamma}\boldsymbol{w}_\nu), \tag{13}$$

where $|\Lambda_I(\boldsymbol{u}_{\kappa I},\boldsymbol{u}_{\nu I})|=|\Lambda_I(\boldsymbol{u}_{\nu I},\boldsymbol{u}_{\kappa I})|\in\mathbb{R}^{4\cdot N_I\times 4\cdot N_I}$ is a block-diagonal symmetric positive semidefinite matrix, and $\boldsymbol{w}_\kappa$ and $\boldsymbol{w}_\nu$ are the entropy variables at the volume nodes of elements κ and ν, respectively. Adding the stabilization term (13) to the entropy-conservative schemes leads to entropy-stable methods, while preserving the conservation and accuracy properties of the original scheme.

V. Results

In this section, we present numerical results validating the conservation, accuracy, and stability properties of the energy- and entropy-stable schemes on non-conforming affine grids. The two-dimensional unsteady isentropic vortex test case with periodic boundary conditions [42] is used for the convergence and efficiency studies and to demonstrate that the schemes are element-wise conservative. This test case is also used to show that entropy is dissipated and conserved using the entropy-conservative schemes (9) and (12) with and without the dissipative term (13), respectively. In order to demonstrate that the energy-stable scheme (8) can conserve and dissipate energy for linear differential equations, we numerically solve a two-dimensional unsteady periodic linear convection problem with symmetric and upwind numerical fluxes, respectively. Finally, to test the robustness of the schemes, we solve a two-dimensional inviscid test case with a discontinuous initial condition.

Although the schemes are applicable on general elements, in this paper, the grids are constructed with triangles. Non-conformity is ensured by randomly assigning different degree operators ($p=1$ to $p=4$) to the elements and by randomly isotropically subdividing some of the elements as shown in Figure 6. Unless otherwise stated, the energy-stable and dense-E entropy-stable schemes use the Ω SBP operators first introduced in [26] and the diagonal-E scheme uses the operators of [13]. The traditional fourth-order Runge-Kutta (RK4) method is utilized to march the solution forward in time with a CFL condition chosen such that the temporal errors are negligible relative to the spatial errors. As previously mentioned, for the energy-stable scheme, we use the Roe flux. For the entropy-conservative schemes, we employ the Ismail and Roe entropy-conservative flux [11] with the extended Taylor series expansion proposed in [14] to compute logarithms near zero. Similar to [14], we define each diagonal block of the symmetric positive semidefinite matrix $|\Lambda_I(\boldsymbol{u}_{\kappa I},\boldsymbol{u}_{\nu I})|$ of the entropy dissipative term (13) as

$$|\Lambda_I([\boldsymbol{u}_{\kappa I}]_l,[\boldsymbol{u}_{\nu I}]_l)|\equiv|\lambda_{\max,n}([\boldsymbol{u}_I^{\text{ave}}]_l)|\frac{\partial\boldsymbol{\mathcal{U}}}{\partial\boldsymbol{\mathcal{W}}}([\boldsymbol{u}_I^{\text{ave}}]_l),\ \forall l=1,...,N_I,$$

where $\lambda_{\max,n}$ is the maximum wave speed in the normal direction and the matrix $\frac{\partial\boldsymbol{\mathcal{U}}}{\partial\boldsymbol{\mathcal{W}}}\in\mathbb{R}^{4\times4}$ is symmetric positive-definite by definition since it is the inverse of the Hessian of the entropy (6a). The values are computed using the arithmetic average of the two states, i.e. $[\boldsymbol{u}_I^{\text{ave}}]_l\equiv\frac{1}{2}([\boldsymbol{u}_{\kappa I}]_l+[\boldsymbol{u}_{\nu I}]_l)$.

[§]Consequently, the mathematical entropy will be non-increasing, which is in accordance with the generation of thermodynamic entropy since the two have opposing signs.

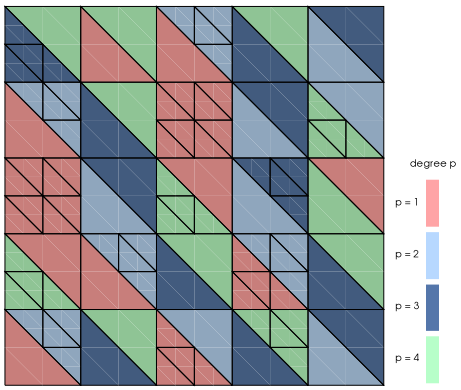

Fig. 6 An example of a coarse non-conforming grid with hanging nodes and different degree operators.

A. Test Cases

1. Isentropic Vortex

The two-dimensional unsteady isentropic vortex problem has an analytical solution given as

$$u = 1 - \frac{\alpha}{2\pi}(y - y_0)e^{1-r^2}, \quad v = \frac{\alpha}{2\pi}\Big(x - (x_0 + t)\Big)e^{1-r^2},$$
$$\rho = \left(1 - \frac{\alpha^2(\gamma-1)}{16\gamma\pi^2}e^{2(1-r^2)}\right)^{\frac{1}{\gamma-1}}, \quad p = \rho^\gamma,$$

where $r^2 = \Big(x - (x_0 + t)\Big)^2 + \Big(y - y_0\Big)^2$, and the vortex strength is set to $\alpha = 3$. The simulation propagates the vortex initially centered at $(x_0, y_0) = (5, 0)$ horizontally to the right on a $[0, 20] \times [-5, 5]$ domain with periodic boundary conditions until $t = 5$. The use of periodic boundary conditions introduces an error since the flow is not uniform at the boundaries (see Section IV.B. of [42] for more details). This error is negligible in our case, because the domain is relatively large.

2. Linear Convection

The two-dimensional unsteady linear convection problem

$$\frac{\partial \mathcal{U}}{\partial t} + a_x\frac{\partial \mathcal{U}}{\partial x} + a_y\frac{\partial \mathcal{U}}{\partial y} = 0,$$

with $a_x = a_y = 1$ and initial condition

$$\mathcal{U}(x, y, 0) = \sin(2\pi x)\sin(2\pi y)$$

is considered. We numerically solve this problem on a $[0, 1]^2$ domain with periodic boundary conditions until $t = 5$. The numerical flux used to couple neighbouring elements is defined as

$$\boldsymbol{f}_n^*([\boldsymbol{u}_{\kappa I}]_l, [\boldsymbol{u}_{\nu I}]_l) \equiv a_n\left(\frac{[\boldsymbol{u}_{\kappa I}]_l + [\boldsymbol{u}_{\nu I}]_l}{2}\right) + \beta\frac{|a_n|}{2}\Big([\boldsymbol{u}_{\kappa I}]_l - [\boldsymbol{u}_{\nu I}]_l\Big), \ \forall l = 1, ..., N_I,$$

where a_n is the velocity in the normal direction, i.e. $a_n = a_x n_x + a_y n_y$. Letting $\beta = 0$ leads to a symmetric flux, while $\beta = 1$ leads to an upwind flux.where a_n is the velocity in the normal direction. Letting $\beta = 0$ leads to a symmetric flux, while $\beta = 1$ leads to an upwind flux.

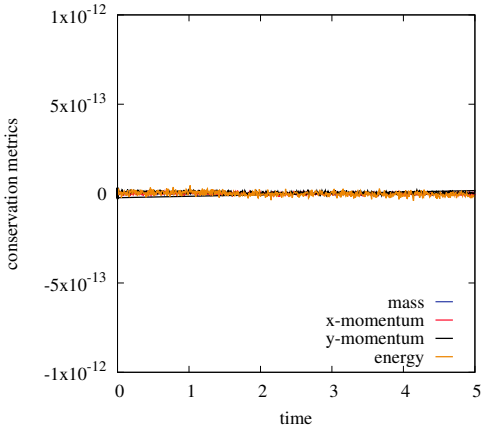

(a) Energy-stable scheme.

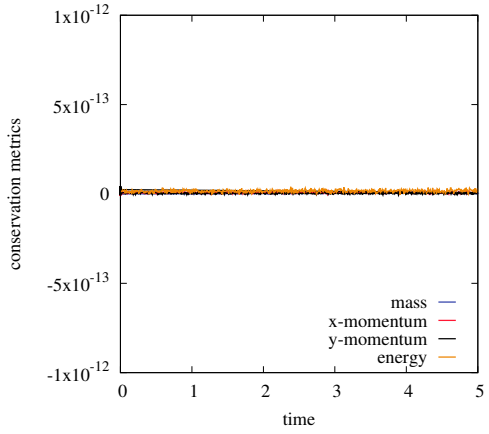

(b) Diagonal-E entropy-stable scheme.

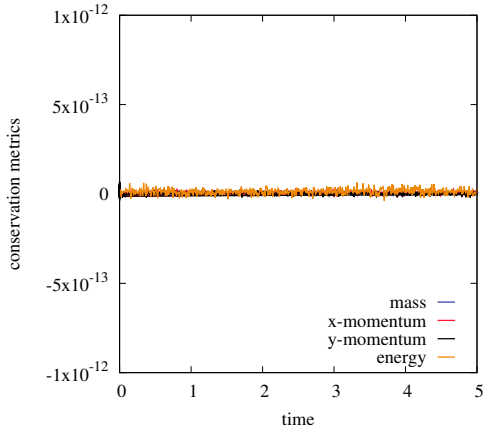

(c) Dense-E entropy-stable scheme.

Fig. 7 Isentropic vortex test case. Mass, momentum, and energy conservation results for the energy- and entropy-stable schemes.

3. Discontinuous Inviscid Problem

For the robustness test case, we solve the two-dimensional Euler equations on a $[0, 20] \times [-5, 5]$ domain with periodic boundary conditions and a discontinuous initial condition defined by

$$\rho = 1.5,\ u = 0.8184,\ v = 0.0,\ p = 0.8032,\ \forall (x, y) \in X,$$
$$\rho = 1.0,\ u = 0.7,\ v = 0.0,\ p = 1.3,\ \forall (x, y) \in \Omega \backslash X,$$

where $X \equiv \{X_a, X_b\}$, $X_a \equiv \{(x, y) \mid 3 \leq x \leq 8, -3 \leq y \leq 3\}$, and $X_b \equiv \{(x, y) \mid 8 \leq x \leq 9, -2 \leq y \leq 2\}$.

B. Conservation

It is important to ensure that the proposed schemes are conservative such that the Lax-Wendroff theorem [43] holds and the schemes can be utilized to simulate flows with discontinuities. To this end, we plot the conservation metrics defined as the discrete integral of the difference in conservative variables at the initial time and time t over the triangulated domain. For instance, for the continuity equation, we have $\sum_{\Omega_\kappa \in \mathcal{T}_h} \mathbf{1}_\kappa^\top \mathsf{H}_\kappa \Big(\boldsymbol{\rho}_\kappa(t) - \boldsymbol{\rho}_\kappa(0) \Big)$. Figure 7

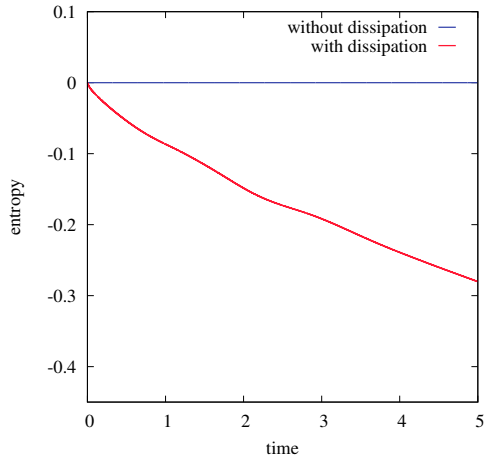

(a) Diagonal-E entropy-stable scheme.

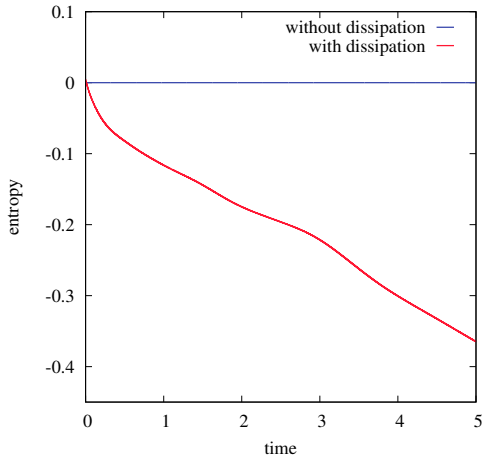

(b) Dense-E entropy-stable scheme.

Fig. 8 Isentropic vortex test case. Entropy conservation and dissipation property of the entropy-conservative and entropy-stable schemes.

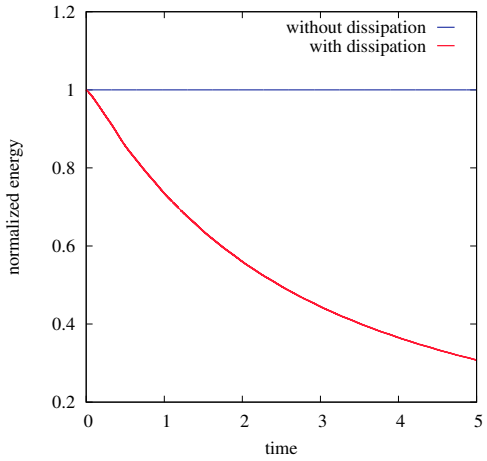

Fig. 9 Linear convection test case. Energy conservation and dissipation property of the energy-stable scheme with symmetric and upwind numerical fluxes.

shows that there is no mass, momentum, or energy generation throughout the duration of the simulation for the energy- and entropy-stable schemes.

C. Entropy and Energy Conservation

To demonstrate that the schemes (9) and (12) can dissipate and conserve entropy with and without the dissipative term, we plot the discrete entropy generation, which is obtained by computing the H-norm inner product between the entropy and conservative variables, i.e. $\sum_{\Omega_\kappa \in \mathcal{T}_h} \boldsymbol{w}_\kappa^\top \tilde{\mathsf{H}}_\kappa \boldsymbol{u}_\kappa$, in Figure 8. Without dissipation, the schemes conserve entropy, while with dissipation entropy decays. The large decrease in entropy is due to the fact that a coarse grid is used in which approximately a quarter of the elements are low order ($p = 1$). Furthermore, the dense-E scheme is more dissipative than the diagonal-E scheme for this test case (note that a common time step was used in order to have a fair comparison between the two runs).

Finally, Figure 9 shows the evolution of discrete energy, computed as $\frac{1}{2} \sum_{\Omega_\kappa \in \mathcal{T}_h} \boldsymbol{u}_\kappa^\top \mathsf{H}_\kappa \boldsymbol{u}_\kappa$, using the energy-stable

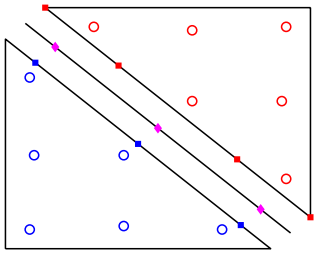

Fig. 10 An Ω ($p = 2$) SBP operator with LG facet quadrature nodes coupled with another Ω ($p = 2$) SBP operator with LGL facet quadrature nodes.

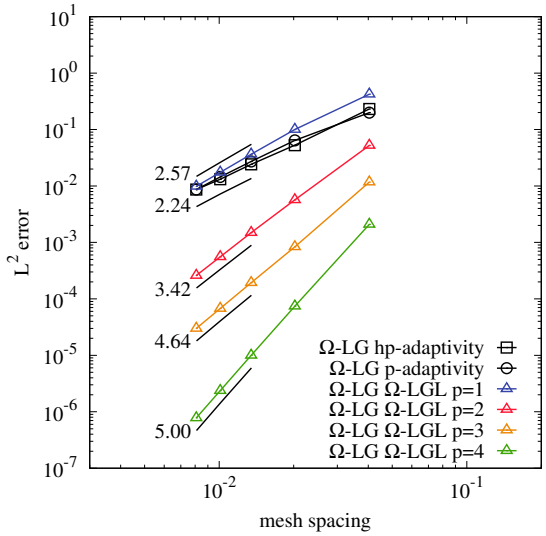

Fig. 11 Isentropic vortex test case. Convergence studies of the energy-stable scheme with the Roe flux.

scheme for the linear convection problem. The results show that energy is conserved with the symmetric flux, and it is dissipated with the upwind flux.

D. Accuracy and Efficiency

We test the accuracy of the schemes on a set of grids with different degree operators without hanging nodes (p-adaptivity) and with hanging nodes (hp-adaptivity), and a set of grids without hanging nodes and constant degree operators but non-conforming facet nodal distributions. An example of the latter is shown in Figure 10 where the LG and LGL facet nodes are used for the two neighbouring elements, respectively[¶]. We utilize grids with $n = 25, 50, 75, 100,$ and 125 right-triangle edges in each direction and approximate the L^2 solution error using the norm matrix as

$$||\boldsymbol{u}^{\text{exact}} - \boldsymbol{u}||_2 \approx ||\boldsymbol{u}^{\text{exact}} - \boldsymbol{u}||_{\mathsf{H}} \equiv \sqrt{\sum_{\Omega_\kappa \in \mathcal{T}_h} (\boldsymbol{u}_\kappa^{\text{exact}} - \boldsymbol{u}_\kappa)^\top \tilde{\mathsf{H}}_\kappa (\boldsymbol{u}_\kappa^{\text{exact}} - \boldsymbol{u}_\kappa)}.$$

Figures 11 and 12 present the convergence study results. The asymptotic convergence rates calculated from the least squares regression line of the 3 finest grids are also shown on the plots. The energy-stable scheme converges at a rate of at least $p_{\text{min}} + 1$ in all cases. The diagonal-E and dense-E entropy-conservative schemes converge at a rate of approximately p_{min} for odd-degree operators (except for the $p = 1$ dense-E scheme which is not believed to be in the asymptotic region). This behaviour has been observed for odd-degree entropy-conservative schemes on conforming grids as well (e.g. [15]). For even-degree operators, the dense-E scheme converges at a rate of $p_{\text{min}} + 1$, whereas the

[¶]For the diagonal-E scheme, the diagonal-E SBP operators with facet LGL nodes introduced in [17] are used.

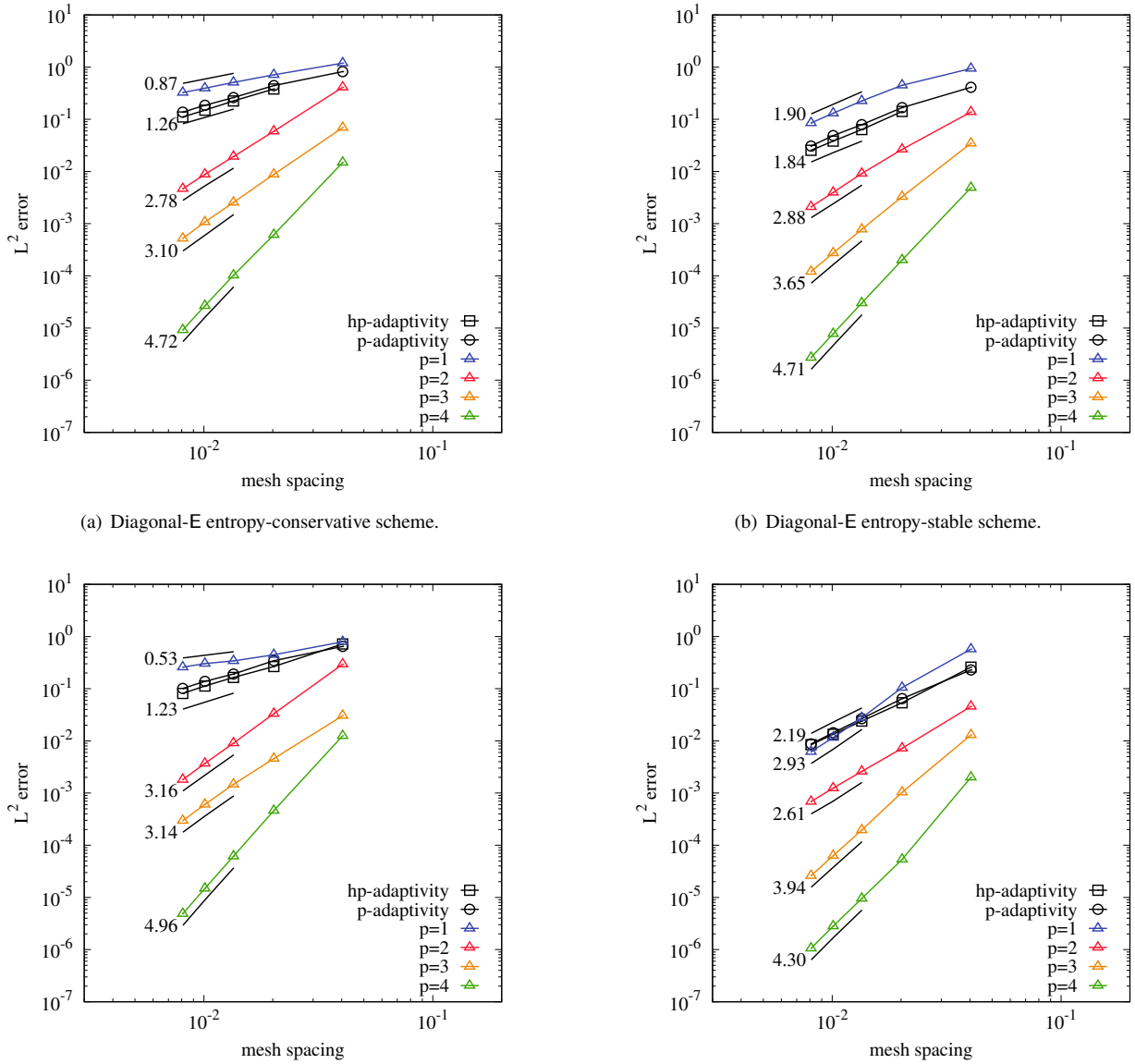

(a) Diagonal-E entropy-conservative scheme.

(b) Diagonal-E entropy-stable scheme.

(c) Dense-E entropy-conservative scheme.

(d) Dense-E entropy-stable scheme.

Fig. 12 Isentropic vortex test case. Convergence studies of the entropy-conservative and entropy-stable schemes.

diagonal-E scheme converges at a rate of $p_{\text{min}} + 0.7$. The latter suboptimal convergence rate is believed to be due to the low accuracy property of diagonal-E operators on simplices. In general, adding the dissipative term increases the convergence rate to at least $p_{\text{min}} + 1$ for the odd-degree operators. For the even-degree diagonal-E scheme, the convergence rate does not change by much although the error decreases on a given grid. In contrast, for the even-degree dense-E scheme, adding dissipation decreases the convergence rate to values between p_{min} and $p_{\text{min}} + 1$; however, lower errors are still achieved on a given grid. This behaviour has also been observed in previous work on conforming entropy-stable schemes (e.g. [14]).

Figure 13 shows a plot of the normalized spatial residual computation time versus the L^2 solution error for the energy-stable (ES) scheme, the entropy-conservative (EC) schemes, and the entropy-stable (SS) schemes. The energy-stable scheme is the most efficient of the five methods, since it computes the actual flux at the volume nodes and the Roe numerical flux at the facet nodes (as opposed to computing relatively more expensive entropy-conservative

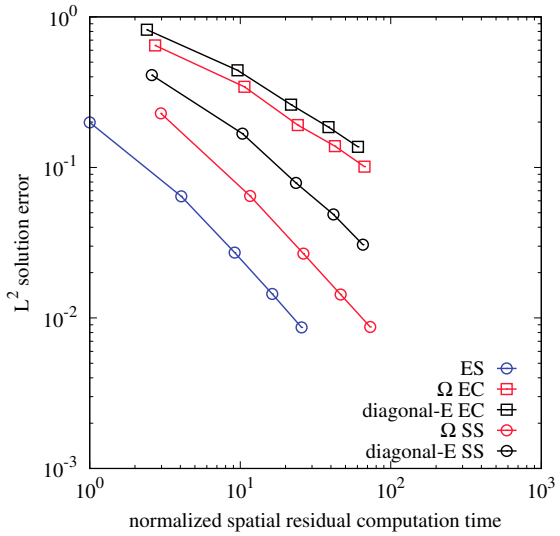

Fig. 13 Isentropic vortex test case. Efficiency of all three schemes.

fluxes at all the volume and facet nodes). The diagonal-E scheme is slightly less computationally expensive than the dense-E scheme, since it couples fewer nodes of neighbouring elements. However, the Ω operators are in general more accurate than the diagonal-E operators and, thus, the dense-E scheme is more efficient (i.e. more accurate for a given CPU time or less computationally expensive for a given error level). Furthermore, adding the stabilization term significantly improves the accuracy of the schemes while having a negligible effect on the computational cost. Finally, the dense-E entropy-stable scheme achieves similar errors as the energy-stable scheme on a given grid.

E. Robustness

The discontinuous inviscid test case described in Section V.A is solved using the energy-stable scheme and the two entropy-stable schemes on a non-conforming grid with 20 right-triangle edges in each direction and degree $p = 3$ and $p = 4$ operators. Some of the elements are randomly h-refined to introduce hanging nodes. As shown in Figure 14, the energy-stable scheme does not provide enough dissipation, and the simulation crashes at $t \approx 1$ for CFL $= \{0.5, 0.25, 0.1, 0.05\}$, while both entropy-stable schemes are stable until the end of the simulation ($t = 5$).

VI. Conclusion

Three high-order, element-wise conservative semi-discrete schemes applicable to non-conforming unstructured grids have been presented. The conservation, stability, and design-order accuracy properties of all three methods were numerically verified. The energy-stable scheme is the most efficient; however it is not provably nonlinearly stable. The second method is entropy-stable and is compatible with diagonal-E SBP operators, which have collocated volume and facet nodes. The third method is also entropy-stable and provides more flexibility since it is compatible with dense-E SBP operators. While this method is slightly more computationally expensive than its diagonal-E counterpart, it is more efficient due to the greater accuracy properties generally provided by dense-E operators. Current work involves augmenting this scheme with the inter-element coupling term employed in [15] to further increase its efficiency. We are also extending these schemes to curved non-conforming grids.

VII. Acknowledgments

We wish to thank the Aerospace Computational Engineering Lab at the University of Toronto for the use of their software, the Automated PDE Solver (APS), and Masayuki Yano for helpful discussions. We are also grateful for the financial support provided by the governments of Ontario and Canada. Computations were performed on the Niagara supercomputer at the SciNet HPC Consortium [44]. SciNet is funded by: the Canada Foundation for Innovation; the Government of Ontario; Ontario Research Fund - Research Excellence; and the University of Toronto.

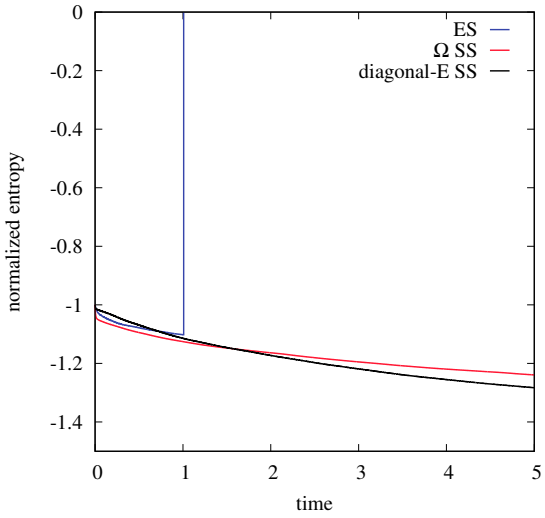

Fig. 14 Discontinuous Euler test case. Evolution of the entropy throughout the simulation for the three different schemes.

References

[1] Liu, C., "High performance computation for DNS/LES," *Applied Mathematical Modelling*, Vol. 30, No. 10, 2006, pp. 1143–1165. doi:10.1016/j.apm.2005.06.013.

[2] Wang, Z. J., Fidkowski, K., Abgrall, R., Bassi, F., Caraeni, D., Cary, A., Deconinck, H., Hartmann, R., Hillewaert, K., Huynh, H. T., Kroll, N., May, G., Persson, P.-O., van Leer, B., and Visbal, M., "High-order CFD methods: current status and perspective," *International Journal for Numerical Methods in Fluids*, Vol. 72, No. 8, 2013, pp. 811–845. doi:10.1002/fld.3767.

[3] Vincent, P. E., Castonguay, P., and Jameson, A., "A New Class of High-Order Energy Stable Flux Reconstruction Schemes," *Journal of Scientific Computing*, Vol. 47, No. 1, 2011, pp. 50–72. doi:10.1007/s10915-010-9420-z.

[4] Zhang, Q., and Shu, C.-W., "Stability Analysis and A Priori Error Estimates of the Third Order Explicit RungeKutta Discontinuous Galerkin Method for Scalar Conservation Laws," *SIAM Journal on Numerical Analysis*, Vol. 48, No. 3, 2010, pp. 1038–1063. doi:10.1137/090771363.

[5] Del Rey Fernández, D. C., Hicken, J. E., and Zingg, D. W., "Review of summation-by-parts operators with simultaneous approximation terms for the numerical solution of partial differential equations," *Computers & Fluids*, Vol. 95, 2014, pp. 171–196.

[6] Svärd, M., and Nordström, J., "Review of summation-by-parts schemes for initial-boundary-value problems," *Journal of Computational Physics*, Vol. 268, 2014, pp. 17–38. doi:10.1016/j.jcp.2014.02.031.

[7] Fisher, T. C., "High-order L2 stable multi-domain finite difference method for compressible flows," Ph.D. thesis, Purdue University, 2012.

[8] Pulliam, T. H., and Zingg, D. W., *Fundamental Algorithms in Computational Fluid Dynamics*, Scientific Computation, Springer International Publishing, Cham, 2014. DOI: 10.1007/978-3-319-05053-9.

[9] Hughes, T., Franca, L., and Mallet, M., "A new finite element formulation for computational fluid dynamics: I. Symmetric forms of the compressible Euler and Navier-Stokes equations and the second law of thermodynamics," *Computer Methods in Applied Mechanics and Engineering*, Vol. 54, No. 2, 1986, pp. 223–234. doi:10.1016/0045-7825(86)90127-1.

[10] Barth, T. J., "Numerical Methods for Gasdynamic Systems on Unstructured Meshes," *An Introduction to Recent Developments in Theory and Numerics for Conservation Laws*, Vol. 5, edited by M. Griebel, D. E. Keyes, R. M. Nieminen, D. Roose, T. Schlick, D. Kröner, M. Ohlberger, and C. Rohde, Springer Berlin Heidelberg, Berlin, Heidelberg, 1999, pp. 195–285. doi:10.1007/978-3-642-58535-7_5.

[11] Ismail, F., and Roe, P. L., "Affordable, entropy-consistent Euler flux functions II: Entropy production at shocks," *Journal of Computational Physics*, Vol. 228, No. 15, 2009, pp. 5410–5436. doi:10.1016/j.jcp.2009.04.021.

[12] Carpenter, M. H., Fisher, T. C., Nielsen, E. J., and Frankel, S. H., "Entropy Stable Spectral Collocation Schemes for the Navier–Stokes Equations: Discontinuous Interfaces," *SIAM Journal on Scientific Computing*, Vol. 36, No. 5, 2014, pp. B835–B867. doi:10.1137/130932193.

[13] Chen, T., and Shu, C.-W., "Entropy stable high order discontinuous Galerkin methods with suitable quadrature rules for hyperbolic conservation laws," *Journal of Computational Physics*, Vol. 345, 2017, pp. 427–461. doi:10.1016/j.jcp.2017.05.025.

[14] Crean, J., Hicken, J. E., Del Rey Fernández, D. C., Zingg, D. W., and Carpenter, M. H., "Entropy-stable summation-by-parts discretization of the Euler equations on general curved elements," *Journal of Computational Physics*, Vol. 356, 2018, pp. 410–438. doi:10.1016/j.jcp.2017.12.015.

[15] Chan, J., "On discretely entropy conservative and entropy stable discontinuous Galerkin methods," *Journal of Computational Physics*, Vol. 362, 2018, pp. 346–374.

[16] Parsani, M., Carpenter, M. H., Fisher, T. C., and Nielsen, E. J., "Entropy Stable Staggered Grid Discontinuous Spectral Collocation Methods of any Order for the Compressible Navier–Stokes Equations," *SIAM Journal on Scientific Computing*, Vol. 38, No. 5, 2016, pp. A3129–A3162. doi:10.1137/15M1043510.

[17] Del Rey Fernández, D. C., Crean, J., Carpenter, M. H., and Hicken, J. E., "Staggered-Grid Entropy-Stable Multidimensional Summation-By-Parts Discretizations on Curvilinear Coordinates," *Journal of Computational Physics (accepted)*, 2019.

[18] Friedrich, L., Schnücke, G., Winters, A. R., Del Rey Fernández, D. C., Gassner, G. J., and Carpenter, M. H., "Entropy Stable Space-Time Discontinuous Galerkin Schemes with Summation-by-Parts Property for Hyperbolic Conservation Laws," *arXiv preprint arXiv:1808.08218 [math]*, 2018.

[19] Parsani, M., Carpenter, M. H., and Nielsen, E. J., "Entropy stable wall boundary conditions for the three-dimensional compressible Navier-Stokes equations," *Journal of Computational Physics*, Vol. 292, 2015, pp. 88–113. doi:10.1016/j.jcp.2015.03.026.

[20] Dalcin, L., Rojas, D. B., Zampini, S., Del Rey Fernández, D. C., Carpenter, M. H., and Parsani, M., "Conservative and entropy stable solid wall boundary conditions for the compressible Navier-Stokes equations: Adiabatic wall and heat entropy transfer," *arXiv preprint arXiv:1812.11403 [physics]*, 2018.

[21] Yano, M., and Darmofal, D. L., "An optimization-based framework for anisotropic simplex mesh adaptation," *Journal of Computational Physics*, Vol. 231, No. 22, 2012, pp. 7626–7649. doi:10.1016/j.jcp.2012.06.040.

[22] Fidkowski, K. J., "Output-based space-time mesh optimization for unsteady flows using continuous-in-time adjoints," *Journal of Computational Physics*, Vol. 341, 2017, pp. 258–277. doi:10.1016/j.jcp.2017.04.005.

[23] Hartmann, R., Held, J., Leicht, T., and Prill, F., "Error Estimation and Adaptive Mesh Refinement for Aerodynamic Flows," *ADIGMA - A European Initiative on the Development of Adaptive Higher-Order Variational Methods for Aerospace Applications*, Vol. 113, edited by E. H. Hirschel, W. Schröder, K. Fujii, W. Haase, B. Leer, M. A. Leschziner, M. Pandolfi, J. Periaux, A. Rizzi, B. Roux, Y. I. Shokin, N. Kroll, H. Bieler, H. Deconinck, V. Couaillier, H. Ven, and K. Sørensen, Springer Berlin Heidelberg, Berlin, Heidelberg, 2010, pp. 339–353. doi:10.1007/978-3-642-03707-8_24.

[24] Friedrich, L., Winters, A. R., Del Rey Fernández, D. C., Gassner, G. J., Parsani, M., and Carpenter, M. H., "An Entropy Stable h/p Non-Conforming Discontinuous Galerkin Method with the Summation-by-Parts Property," *Journal of Scientific Computing*, Vol. 77, 2018, pp. 689–725. doi:10.1007/s10915-018-0733-7.

[25] Hicken, J. E., Del Rey Fernández, D. C., and Zingg, D. W., "Multidimensional Summation-by-Parts Operators: General Theory and Application to Simplex Elements," *SIAM Journal on Scientific Computing*, Vol. 38, No. 4, 2016, pp. A1935–A1958. doi:10.1137/15M1038360.

[26] Del Rey Fernández, D. C., Hicken, J. E., and Zingg, D. W., "Simultaneous Approximation Terms for Multi-dimensional Summation-by-Parts Operators," *Journal of Scientific Computing*, Vol. 75, 2017, pp. 83–110. doi:10.1007/s10915-017-0523-7.

[27] Friedrich, L., Del Rey Fernández, D. C., Winters, A. R., Gassner, G. J., Zingg, D. W., and Hicken, J., "Conservative and Stable Degree Preserving SBP Operators for Non-conforming Meshes," *Journal of Scientific Computing*, Vol. 75, No. 2, 2018, pp. 657–686. doi:10.1007/s10915-017-0563-z.

[28] Chan, J., Del Rey Fernández, D. C., and Carpenter, M. H., "Efficient entropy stable Gauss collocation methods," *arXiv preprint arXiv:1809.01178*, 2018.

[29] Gassner, G. J., "A Skew-Symmetric Discontinuous Galerkin Spectral Element Discretization and Its Relation to SBP-SAT Finite Difference Methods," *SIAM Journal on Scientific Computing*, Vol. 35, No. 3, 2013, pp. A1233–A1253. doi:10.1137/120890144.

[30] Lundquist, T., and Nordström, J., "On the suboptimal accuracy of summation-by-parts schemes with non-conforming block interfaces," Tech. rep., Linköping University, 2015.

[31] Friedrichs, K. O., and Lax, P. D., "Systems of conservation equations with a convex extension," *Proceedings of the National Academy of Sciences*, Vol. 68, No. 8, 1971, pp. 1686–1688.

[32] Dafermos, C. M., *Hyperbolic Conservation Laws in Continuum Physics*, 3rd ed., Vol. 325, Springer Berlin Heidelberg, 2010.

[33] Svärd, M., "Weak solutions and convergent numerical schemes of modified compressible NavierStokes equations," *Journal of Computational Physics*, Vol. 288, 2015, pp. 19–51. doi:10.1016/j.jcp.2015.02.013.

[34] Harten, A., "On the symmetric form of systems of conservation laws with entropy," *Journal of Computational Physics*, Vol. 49, No. 1, 1983, pp. 151–164. doi:10.1016/0021-9991(83)90118-3.

[35] Tadmor, E., "Skew-selfadjoint form for systems of conservation laws," *Journal of Mathematical Analysis and Applications*, Vol. 103, No. 2, 1984, pp. 428–442. doi:10.1016/0022-247X(84)90139-2.

[36] Tadmor, E., "The numerical viscosity of entropy stable schemes for systems of conservation laws. I," *Mathematics of Computation*, Vol. 49, No. 179, 1987, pp. 91–103.

[37] Chandrashekar, P., "Kinetic energy preserving and entropy stable finite volume schemes for compressible Euler and Navier-Stokes equations," *Communications in Computational Physics*, Vol. 14, No. 5, 2013, pp. 1252–1286.

[38] Ranocha, H., "Comparison of Some Entropy Conservative Numerical Fluxes for the Euler Equations," *Journal of Scientific Computing*, Vol. 76, No. 1, 2018, pp. 216–242. doi:10.1007/s10915-017-0618-1.

[39] Roe, P. L., "Approximate Riemann Solvers, Parameter Vectors, and Difference Schemes," *Journal of Computational Physics*, Vol. 135, 1981, pp. 357–372.

[40] LeFloch, P. G., Mercier, J. M., and Rohde, C., "Fully Discrete, Entropy Conservative Schemes of Arbitrary Order," *SIAM Journal on Numerical Analysis*, Vol. 40, No. 5, 2002, pp. 1968–1992. doi:10.1137/S003614290240069X.

[41] Fisher, T. C., and Carpenter, M. H., "High-order entropy stable finite difference schemes for nonlinear conservation laws: Finite domains," *Journal of Computational Physics*, Vol. 252, 2013, pp. 518–557. doi:10.1016/j.jcp.2013.06.014.

[42] Spiegel, S. C., Huynh, H. T., DeBonis, J. R., and Glenn, N., "A survey of the isentropic Euler vortex problem using high-order methods," *22nd AIAA Computational Fluid Dynamics Conference, AIAA Aviation*, 2015, pp. 1–21.

[43] Lax, P., and Wendroff, B., "Systems of conservation laws," *Communications on Pure and Applied Mathematics*, Vol. 13, No. 2, 1960, pp. 217–237.

[44] Loken, C., Gruner, D., Groer, L., Peltier, R., Bunn, N., Craig, M., Henriques, T., Dempsey, J., Yu, C.-H., Chen, J., Dursi, L. J., Chong, J., Northrup, S., Pinto, J., Knecht, N., and Zon, R. V., "SciNet: Lessons Learned from Building a Power-efficient Top-20 System and Data Centre," *Journal of Physics: Conference Series*, Vol. 256, 2010, p. 012026. doi:10.1088/1742-6596/256/1/012026.

A. Construction of the Interface Interpolation and Projection Operators

A. Interpolation Operators

Defining n_{r_κ} as the cardinality of the monomial basis of total degree r_κ, let $\mathsf{V}_\kappa \in \mathbb{R}^{N_\kappa \times n_{r_\kappa}}$ be the degree r_κ full-column-rank Vandermonde matrix evaluated at the volume nodes of the (reference) element κ, $\mathsf{V}_{\kappa\gamma} \in \mathbb{R}^{N_{\kappa\gamma} \times n_{r_\kappa}}$ the degree r_κ full-column-rank Vandermonde matrix evaluated at the (reference) facet nodal set $S_{\kappa\gamma}$, and $\mathsf{V}_{\kappa I} \in \mathbb{R}^{N_I \times n_{r_\kappa}}$ the degree r_κ full-column-rank Vandermonde matrix evaluated at the (reference) facet nodal set of S_I. We can then construct the interpolation operators $\mathsf{R}_{\kappa\gamma}$ and $\mathsf{P}_{\kappa\gamma\to I}$ as

$$\begin{aligned} \mathsf{R}_{\kappa\gamma} &= \mathsf{V}_{\kappa\gamma}\mathsf{V}_\kappa^\dagger, \quad \text{and} \\ \mathsf{P}_{\kappa\gamma\to I} &= \mathsf{V}_{\kappa I}\mathsf{V}_{\kappa\gamma}^\dagger, \end{aligned}$$

where $\dagger$ denotes the Moore-Penrose pseudo-inverse, e.g. $\mathsf{A}^\dagger \equiv (\mathsf{A}^\top\mathsf{A})^{-1}\mathsf{A}^\top$ for a non-square matrix A with full column rank. The interpolation operator $\mathsf{P}_{\nu\gamma\to I}$ can be constructed similarly.

B. Projection Operators

The first entropy-stable scheme uses the operators $\mathsf{P}_{\kappa\gamma\to\nu\gamma}$ and $\mathsf{P}_{\nu\gamma\to\kappa\gamma}$. As previously mentioned, $\mathsf{P}_{\nu\gamma\to\kappa\gamma}$ can be split into the interpolation operator $\mathsf{P}_{\nu\gamma\to I}$ and the projection operator $\mathsf{P}_{\kappa\gamma\to I}$, mainly $\mathsf{P}_{\nu\gamma\to\kappa\gamma} = \mathsf{P}_{I\to\kappa\gamma}\mathsf{P}_{\nu\gamma\to I}$. We define the projection operator $\mathsf{P}_{I\to\kappa\gamma}$ such that

$$(\boldsymbol{v}, \boldsymbol{f}_I)_{\mathsf{B}_{\kappa\gamma}} = (\boldsymbol{v}, \boldsymbol{f}_I)_{\mathsf{B}_I}, \quad \forall\, \boldsymbol{v} \in \mathbb{P}_{r_\kappa}(\partial\Omega_{\kappa\gamma}),$$

where $\boldsymbol{f}_I \in \mathbb{R}^{N_I}$ holds the evaluation of an L^2 integrable function $\mathcal{F}(x, y)$ at the set S_I. The inner products can be equivalently written in matrix form as

$$\boldsymbol{v}_{\kappa\gamma}^\top \mathsf{B}_{\kappa\gamma}\mathsf{P}_{I\to\kappa\gamma}\boldsymbol{f}_I = \boldsymbol{v}_{\kappa\gamma}^\top \mathsf{P}_{\kappa\gamma\to I}^\top \mathsf{B}_I \boldsymbol{f}_I, \quad \forall \boldsymbol{v} \in \mathbb{P}_{r_\kappa}(\Omega_{\kappa\gamma}),$$

Since this equality holds for any arbitrary function $\mathcal{F}(x, y) \in L^2(\Omega)$ and for all $\boldsymbol{v} \in \mathbb{P}_{r_\kappa}(\partial\Omega_{\kappa\gamma})$, we can enforce

$$\mathsf{B}_{\kappa\gamma}\mathsf{P}_{I\to\kappa\gamma} = \mathsf{P}_{\kappa\gamma\to I}^\top \mathsf{B}_I,$$

by defining $\mathsf{P}_{I\to\kappa\gamma}$ as

$$\mathsf{P}_{I\to\kappa\gamma} \equiv \mathsf{B}_{\kappa\gamma}^{-1}\mathsf{P}_{\kappa\gamma\to I}^\top \mathsf{B}_I.$$

The projection operator $\mathsf{P}_{I\to\nu\gamma}$ can be defined similarly. These definitions are similar to the ones presented in [27] for tensor-product LGL operators.